

Eutectic Solidification Morphologies in Rapidly Solidified Hypereutectic Sn–Ag Solder Alloy



HUAMAO RAO, ANDREW MULLIS, and ROBERT COCHRANE

The effect of rapid solidification upon hypereutectic Sn–Ag solder alloy has been investigated using a 6.5 m drop tube. Powder sizes ranging from > 850 to $< 38 \mu\text{m}$ were produced, with equivalent cooling rates of 250 to $14,800 \text{ K s}^{-1}$ for 850 and $38 \mu\text{m}$ droplets, respectively. At all cooling rates investigated, dendritic β -Sn was observed as the primary solidification phase, not proeutectic Ag_3Sn as predicted by the phase diagram. The volume fraction of interdendritic eutectic was observed to decrease with increasing cooling rate, with the Ag concentration in the residual interdendritic liquid estimated at 12.5 – 15 wt pct Ag , far in excess of the eutectic concentration of 3.8 wt pct . Much of the Ag_3Sn observed within the eutectic had a blocky, divorced eutectic appearance. A model is proposed which can explain these observations in terms of sluggish nucleation of the Ag_3Sn intermetallic, coupled with a metastable phase diagram that permits significant supersaturation of Ag at modest undercooling.

<https://doi.org/10.1007/s11661-024-07579-2>
© The Author(s) 2024

I. INTRODUCTION

THE excellent mechanical properties of lead-tin solder have made it a mainstay in electronic soldering since the dawn of the electronics age. However, due to the toxicity of lead, and its propensity to leach from waste electronics into ground water, more environmentally friendly solders that mimic the mechanical reliability of Pb–Sn solder are required.^[1] Lead-free solders, including Sn–Ag and Sn–Ag–Cu are used extensively as alternatives to traditional Pb–Sn solder due to their excellent mechanical and electrical properties. The eutectic point of Sn– 3.5 wt pct Ag solder is 494 K , the low melting point providing excellent soldering performance, while the evenly dispersed intermetallic (Ag_3Sn) in the solder provides good mechanical strength.^[2]

The exploration of the eutectic-coupled zone is particularly important for control of the microstructure in solders. The coupled zone is a measure of the range of composition, interfacial velocity, and temperature over which a fully eutectic structure grows.^[3–8] However, the nature of the solid–liquid (S/L) interface for the two (or more) phases present in the eutectic strongly influences the nature of the coupled zone. The entropy of melting, ΔS_m , defined as the entropy difference between the solid

and liquid phases at the melting point, determines the S/L interface structure. The atomic roughness of the solid–liquid interface at equilibrium is characterized by the Jackson factor,^[9] $\alpha = \Delta S_m/R$, where R is the gas constant. Croker and co-workers (see *e.g.*^[10–14]) have calculated the Jackson factor for a wide range of systems and through analysis of the microstructures, $\alpha = 2.7$ was used to distinguish between non-faceted and faceted phases. With $\alpha > 2.7$, the S/L interface is atomically smooth with a small number of ledges to aid atomic attachment. Since growth occurs by atoms attaching at these ledges, the ledge sweeps across the crystal normal to the growth direction, meaning that growth perpendicular to the plane is very slow. This ultimately limits the growth rate of such crystals, resulting in a faceted morphology at the macroscopic scale and often a requirement for high undercooling for nucleation and growth. Conversely, in the case of $\alpha < 2.7$, the S/L interface is atomically rough, with many sites at which atoms can attach. Therefore, the crystal will form a non-faceted phase.^[15] A non-faceted–non-faceted (nf–nf) eutectic exhibits a lamellar or rod-like eutectic microstructure (depending upon the relative volume fractions of the phases) and a phase diagram displaying a broadly symmetrical coupled zone below the eutectic point. Such systems include Pb–Sn, Pb–Cd, and Ag–Cu. Conversely, most eutectic systems including an intermetallic phase, such as Fe– Fe_3C , Co–Mo ($\text{Co–Co}_7\text{Mo}_6$) or Sn–Ag ($\text{Sn–Ag}_3\text{Sn}$) or a non-metallic end member, such as Al–Si, display faceted–non-faceted (f–nf) or irregular eutectics.^[5] In such cases, the coupled zone is generally skewed significantly towards the side of the phase diagram containing the faceted phase.^[16]

HUAMAO RAO, ANDREW MULLIS, and ROBERT COCHRANE are with the School of Chemical & Process Engineering, University of Leeds, Leeds LS2 9JT UK. Contact e-mail: ml19h2r@leeds.ac.uk

Manuscript submitted June 11, 2024; accepted August 24, 2024.

Article published online September 13, 2024

Rapid solidification techniques result in alloys with significant microstructural and compositional changes.^[17] Extended solid solubility and metastable phase formation are among some of the effects to be demonstrated at large departures from equilibrium. Li *et al.*^[18] observed solute trapping in Al–Cu–Mg–Mn–Zr alloy during laser powder bed fusion (L-PBF). Under the non-equilibrium conditions occasioned by rapid solidification, the reduced diffusion of elements inhibited the formation of the Al₃Zr phase, causing Zr solute to be trapped in the Al matrix. Wang *et al.*^[19] and Bathula *et al.*^[20] studied Al–Cu alloys using wedge copper mold casting and laser melting techniques, respectively. Solute trapping occurred in the Al matrix in both cases. However, the solute trapping observed by Bathula *et al.*^[20] was more profound and this, combined with high cooling rates, resulted in the formation of metastable θ -Al₂Cu.

Rapid solidification also typically results in microstructural refinement. Ni–Cu is one of many systems reported to display grain refinement under non-equilibrium conditions,^[21–24] with mechanisms including dendritic fragmentation and recrystallization having been proposed. During the rapid solidification of eutectics, this scale refinement often manifests as a reduction in lamellar spacing and a breakdown of eutectic growth in favor of single-phase dendrites. In the case of f–nf systems, there is a tendency for the non-faceted phase to be favored, either at the eutectic composition or off-eutectic when the phase diagram suggests the faceted phase should form the proeutectic. Abul *et al.*^[25] found that in a Al–2.85 wt pct Fe alloy (equilibrium eutectic Al–Al₁₃Fe₄ at 1.7 wt pct Fe), rapid cooling changed the dominant microstructure from one containing blocky proeutectic Al₁₃Fe₄ and an irregular eutectic containing long Al₁₃Fe₄ needles, to one dominated by primary α -Al dendrites and a regular interdendritic eutectic. This is consistent with the results reported by Qi *et al.*^[26] using laser powder bed fusion. However, Qi *et al.* found only needle-like intermetallics distributed in an Al matrix, rather than the transformation of the bulk intermetallic into a regular lamellar eutectic as reported by Abul *et al.*^[25]. Lien *et al.*^[27] and Wei *et al.*^[28] performed laser surface melting experiments on the Al–20 wt pct Si hypereutectic system, finding rapid solidification resulted in the formation of primary α -Al and an interdendritic eutectic, instead of primary Si.

This favoring of the non-faceted phase is also observed in hypereutectic Sn–Ag alloys, which exhibit the formation of primary β -Sn and Sn–Ag₃Sn eutectic during rapid solidification.^[29,30] Bromley *et al.* and Sahin *et al.*^[31,32] established the relationship between growth rate and eutectic microstructure of near eutectic Sn–Ag alloys. At relatively high growth rates, a rod-like eutectic structure is promoted, while a plate-like intermetallic is formed if the growth rate is lower. Microstructural refinement due to rapid solidification has similarly been demonstrated in these alloys,^[29] as well as changes in the morphology of the intermetallic within the eutectic.^[33–35]

Cooperative eutectic growth cannot be observed when the proportion of residual liquid is so small that the width of the liquid channel is comparable to the eutectic spacing. In this case, the minority phase (by volume) is more likely to form single particles or lamellae in the residual liquid. This is the classic divorced eutectic.^[36] Numerous publications have reported different mechanisms for the formation of divorced eutectic.^[37–41] For example, Kang *et al.*^[38] used phase-field simulation and a thermodynamic model to study the Al–Mg alloy system. Solute trapping and uncoupled growth caused by large departures from equilibrium led to the formation of a structure resembling the classic divorced eutectic. Baral *et al.*^[39] found that the addition of Zn promoted the formation of divorced eutectic in Al–Mg alloy and suggested that Zn changed the phase distribution so as to promote this morphology. Similarly, in the Ti–C system, it is proposed that the formation of divorced eutectic is related to solute segregation and grain refinement.^[40] A high cooling rate leads to a reduction in grain size and solute segregation promotes the formation of fine eutectic structure. Ultimately, eutectic growth is inhibited and a divorced eutectic is formed.^[40] A seemingly divorced eutectic microstructure was also reported by Liao *et al.*^[41] using glass tube suction casting while studying the A390 alloy system (Al with hypereutectic Si + multiple other additions). However, they found that due to the low cooling rate, sufficient undercooling was not achieved to nucleate Si in the eutectic, but rather that Si deposition was preferred on existing Si cells, giving a microstructure similar in appearance to a divorced eutectic, albeit the volume fraction of residual liquid at the eutectic was not particularly small.

In this paper, we utilize the drop-tube technique to investigate the impact of rapid solidification, comprising both high cooling rate and deep undercooling due to containerless solidification of droplets in flight, on the microstructural development of a near eutectic Sn–Ag solder alloy.

II. EXPERIMENTAL METHODS

A. Sample Preparation and Characterization

A commercial hypereutectic solder alloy of nominal composition Sn–4.0 wt pct Ag is used as the raw material for the drop-tube experiment and also acts as a reference material for benchmarking the effects of rapid solidification. Approximately 7.5 g of the Sn–4 wt pct Ag alloy was placed in an open-top alumina crucible which had three 300 μ m laser-drilled holes in the base. The crucible was then positioned inside a graphite susceptor to facilitate induction heating, surrounded by two cylindrical alumina heat shields. This crucible assembly was then placed within the drop-tube furnace chamber such that it can be pressurized independently of its surroundings so as to eject a spray of molten droplets once melting is complete. A schematic of the drop-tube apparatus is shown in Figure 1.

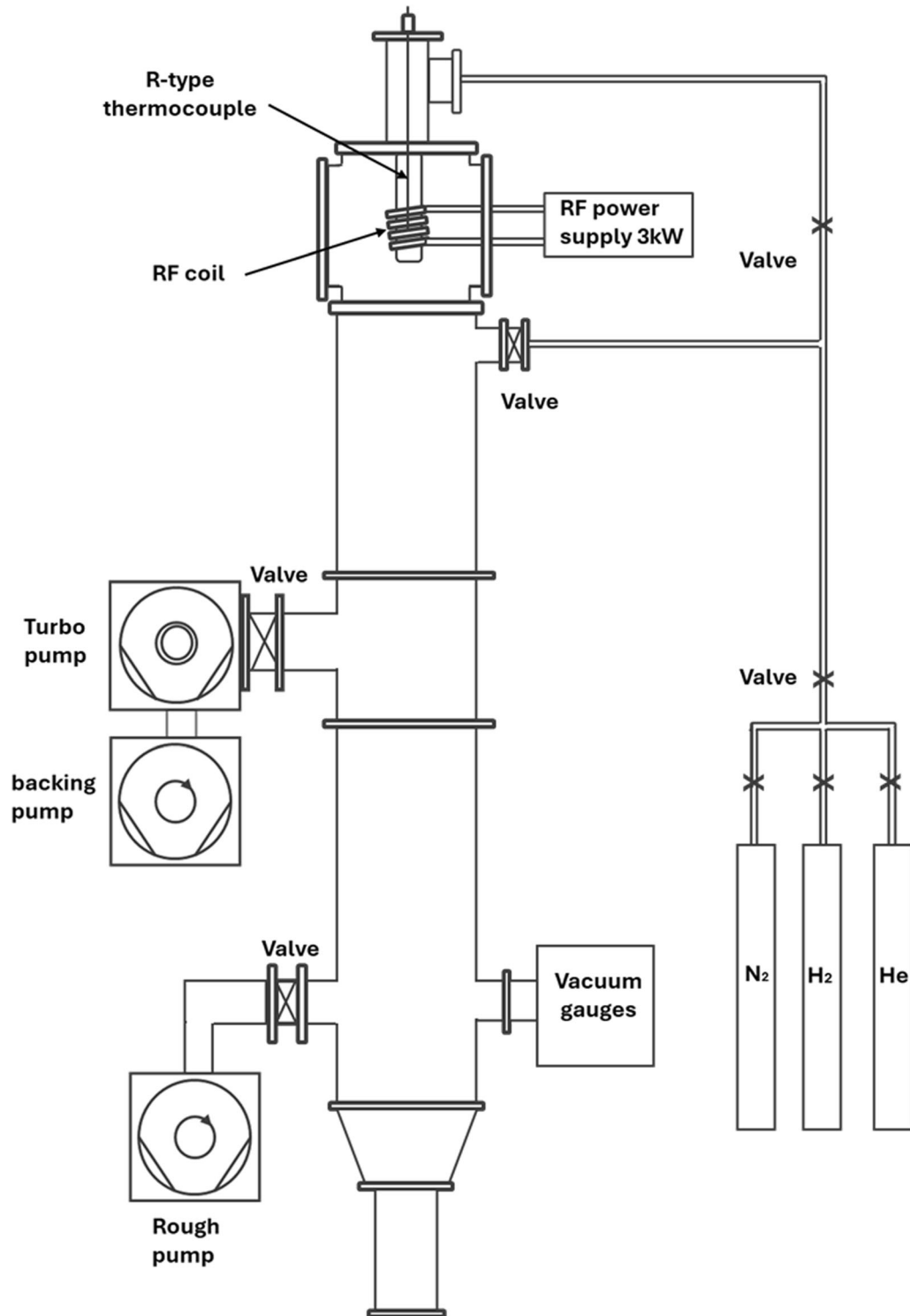


Fig. 1—Schematic diagram of the drop tube from University of Leeds.

In order to ensure an oxygen-free environment for solidification, the drop tube was evacuated using a 2-stage oil-sealed rotary vacuum pump, with an ultimate pressure of 1 Pa being attained before the tube was backfilled with nitrogen gas at a pressure of 40 kPa. This pump-flush cycle was then repeated a further two times before a final evacuation to a pressure of 10^{-4} Pa using

a turbomolecular pump. The tube was then again filled with nitrogen to a pressure of 40 kPa which provides cooling for the molten droplets once ejected. Melting was done by RF induction heating, with a k-type thermocouple mounted inside the crucible just above the melt surface for temperature determination. At a superheat of around 50 K, the crucible was pressurized to

0.4 MPa with nitrogen gas to eject the melt, wherein solidification into droplets of various sizes occurs in free fall within the tube. Following cooling, the droplets were collected and sieved into 10 size fractions, namely: > 850, 850-500, 500-300, 300-212, 212-150, 150-106, 106-75, 75-53, 53-38, and < 38 μm .

Subsequent to droplet collection, the powders were mounted using Buehler EpoThin™ 2 epoxy resin and then ground and polished for microscopic analysis. Grinding was performed sequentially using P400, P600, P1200, and P2500 SiC paper. Following grinding, 3 and 1 μm diamond pastes were used to polish the samples. To achieve a scratch-free surface on the very soft Sn-based solders, a final polishing step using 0.05 μm colloidal silica was employed. The surface of the samples was cleaned with running water and isopropanol.

Preliminary microstructural analysis was performed using an Olympus BX51 optical microscope. Following optical microscopy samples were carbon coated for SEM analysis, performed using either a Hitachi TM3030Plus SEM or Hitachi Su8230 SEM, both equipped with built-in EDX (energy-dispersive X-ray) analyzer. Further examination of the samples was performed on selected areas using an FEI Titan3 Themis 300 TEM. TEM sample preparation was performed using a FEI nova 200 Nanolab FEGSEM with focused ion beam (FIB). The image processing software ImageJ was utilized to determine the volume fraction of both β -Sn dendrites and interdendritic eutectic, making use of the thresholding function to resolve the difference in gray-level contrast between these phases as revealed in the SEM. This program was also used to determine the average eutectic spacing and hence calculate the ratio, ϕ , between the average measured eutectic spacing and the extremum spacing, as required by the Jackson and Hunt^[42] theory for the growth of irregular eutectics. CrysTBox software was used to accelerate the analysis of TEM images due to its highly accurate automated analysis. The DiffractGUI tool in CrysTbox was used to automatically analyze the diffraction patterns for the Sn and Ag₃Sn phases, in particular indexing individual diffraction spots and measuring interplanar angles and distances. Differential scanning calorimetry (PerkinElmer DSC 8000) was used to study the melting of the eutectic. The maximum temperature of the heating program was set to 235 °C, which is slightly higher than tin melting temperature but lower than alloy liquidus to avoid melting the Ag₃Sn intermetallic. To speed up the experiment, a fast heating rate of 20 K/min was used up to 215 °C, which is lower than eutectic point, with a slow heating rate of 1 K/min operating between 215 and 235 °C. This slower heat rate ensures the complete melting of each phase and avoids peak overlap from the different phases.

B. Calculation of Cooling Rate, Phase Diagram, and Coupled Zone

The cooling rate for isolated droplets in free fall can be estimated by calculation of the heat transfer to the surrounding gas at ambient temperature.^[43,44] The heat balance may be expressed as follows:

$$\begin{aligned} \frac{dT}{dt} [C_p^l(1-f) + C_p^s f] + L \frac{df}{dt} \\ = \frac{6}{d\rho_l} [\varepsilon\sigma_{SB}(T^4 - T_R^4) + (h_m(T - T_R))], \end{aligned} \quad [1]$$

where d is the droplet diameter, C_p^l is the specific heat of the melt, C_p^s the specific heat of the solid, f is the solid fraction, L the latent heat, ρ_l the density of the melt, ε the surface emissivity of the melt, σ_{SB} is the Stehan-Boltzman constant, T the instantaneous temperature of the droplet, T_R the temperature of the gas (room temperature), and h_m is the heat transfer coefficient of the droplet falling through a gas. h_m is given by

$$h_m = \frac{\kappa^g}{d} (2.0 + 0.6\sqrt{Re}\sqrt[3]{Pr}), \quad [2]$$

where κ^g is the thermal conductivity of the gas, Re is the Reynolds number and Pr the Prandtl number, with the Reynolds and Prandtl numbers being given by

$$Re = \frac{v^r \rho^g D}{\eta^g}, \quad [3]$$

$$Pr = \frac{C_p^g \eta^g}{\kappa^g}. \quad [4]$$

Here, ρ^g is the density, η^g the dynamic viscosity, and C_p^g the specific heat of the back-fill gas. v^r is the relative velocity between particle and gas, which is taken as the terminal velocity for a freely falling sphere of diameter d , with full details of the calculation of v^r in the context of the heat balance calculation, as given in the reference.^[44] Table I gives the thermophysical parameters assumed for this calculation.

The equilibrium Sn–Ag phase diagram is well established, but the metastable extensions of the liquidus lines for the β -Sn and Ag₃Sn phase are much less so. In order to determine these metastable extensions, which will be useful in interpreting the results of this investigation, the CALPHAD program MTDATA^[45] has been used, together with thermodynamic descriptions of the phases obtained from the SGTE solutions database.

Unlike the calculation of the metastable extensions of the liquidus lines, the calculation of the eutectic-coupled zone is a dynamic, rather than thermodynamic, calculation. That is, it involves the calculation of both the dendritic and the eutectic growth velocities over a range of temperature–composition space below the equilibrium eutectic temperature. The eutectic-coupled zone is then defined as the region where eutectic growth outpaces the growth of either phase individually.

To calculate the growth rate for single-phase dendrites, we use the high Peclet number model originally proposed by Lipton *et al.*^[49] This is based upon the principle of resolving the total undercooling, ΔT , into its thermal, ΔT_t , constitutional, ΔT_c , curvature, ΔT_r , and kinetic, ΔT_k , contributions, such that

Table I. Thermophysical Parameters for N₂ Gas and Tin^[46,47]

Material	Parameter (Unit)	Value
Nitrogen gas ^[48]	C_p^g (J kg ⁻¹ K ⁻¹)	1039
	η^g (N s m)	1.78×10^{-5}
	κ^g (W m ⁻¹ K ⁻¹)	2.6×10^{-2}
	ρ^g (kg m ⁻³)	1.16
Tin	C_p^l (J kg ⁻¹ K ⁻¹)	210
	L (Kkg ⁻¹) (K kg ⁻¹)	58500
	ρ_l (Jkg ⁻¹) (J kg ⁻¹)	7310

$$\Delta T = \Delta T_t + \Delta T_c + \Delta T_r + \Delta T_k, \quad [5]$$

where ΔT_t and ΔT_c are given by the Ivantsov solution for a parabolic needle dendrite under thermal and solutal control, respectively, ΔT_r is a manifestation of the Gibbs-Thomson effect, and the kinetic undercooling is a term proportional to growth velocity. Standard expressions for the terms on the right of Eq. [6] are given in the references^[49] and, for the sake of brevity, are not reproduced here. However, as with all models of this type, there is an issue in that the solution for the undercooling is a function of the Peclet number and as such is degenerate in the product VR where V is the growth velocity of the dendrite tip (the quantity that we seek) and R is the radius of curvature of the tip. To break the degeneracy, we continue to follow Lipton *et al.* by writing

$$R = \frac{1}{\sigma^*(G_c \cdot \zeta_c - G_t \cdot \zeta_t)}, \quad [6]$$

where G_t and G_c are the thermal and solutal gradients at the dendrite tip, and ζ_t and ζ_c are the thermal and solutal modulation factors. This formulation is a high Peclet number modification of the Mullins–Sekerka analysis, where the dendrite tip radius is equated to the shortest wavelength perturbation that is stable under local growth conditions. As above, standard expression for these quantities is given by Lipton *et al.* and so has not been reproduced here. σ^* is a stability constant which is termed as the dendrite tip selection parameter. In the original Mullins–Sekerka analysis $\sigma^* = \frac{1}{4\pi^2} = 0.0253$, while Glicksman *et al.*^[50] obtained a slightly lower value of 0.0192 during microgravity experiments in low Earth orbit. However, the advent of microscopic solvability theory by authors such as Kessler *et al.*^[51] has demonstrated that σ^* is in fact an eigenvalue of the crystalline anisotropy of the growing solid. While providing an elegant theoretical framework, this poses the problem that the crystalline anisotropy at the solid–liquid interface is unknown for almost all alloys. Consequently, in this work, we take the pragmatic approach of setting $\sigma^* = \frac{1}{4\pi^2}$.

During solidification, the kinetic undercooling, $\Delta T_k = V/\mu$, where μ is the kinetic coefficient, will depend on the nature of the phase that is growing. For pure metals, μ is large, and hence, ΔT_k is usually

negligible, except at very high undercooling. Conversely, for intermetallic compounds, particularly those that display faceted growth, μ is small resulting in large ΔT_k . Unfortunately, we can find no information that allows a sensible estimate of μ for the growth of Ag₃Sn from a Sn–Ag melt. Consequently, here we restrict ourselves to the calculation of the coupled zone boundary between the growth of β -Sn and the eutectic, for which we assume the kinetic undercooling is negligible.

The theory of eutectic growth for regular lamellar and rod-like eutectic was first developed in the classic paper by Jackson and Hunt,^[42] with this subsequently being modified for irregular nf–f type eutectics by Magnin *et al.*^[52] who measured the average undercooling and lamellar spacing to determine the extent of the deviation from the $\lambda^2 V = \text{constant}$ relationship proposed by Jackson and Hunt. The equations for irregular eutectic growth may be written as follows:

$$\lambda_a^2 V = \phi^2 K_2 / K_1, \quad [7]$$

$$\Delta T / \sqrt{V} = (\phi + 1/\phi) \sqrt{K_1 K_2}, \quad [8]$$

$$\lambda_a \Delta T = (\phi^2 + 1) K_2, \quad [9]$$

$$\phi = \lambda_a / \lambda_e, \quad [10]$$

where K_1 and K_2 are the eutectic materials constants as given by Jackson and Hunt, λ_a is the average measured eutectic spacing, and ϕ is an operating parameter which is the ratio between the average measured eutectic spacing and the extremum spacing, λ_e , as given by the Jackson and Hunt model for a regular eutectic.

The parameters used in the evaluation of the model are given in Table II.

III. RESULTS

A. Simulation Results

Figure 2 shows the estimated cooling rate, as a function of droplet diameter, for droplets in the

Table II. Parameters for the Calculation of the Sn–Ag₃Sn Eutectic^[46,53]

Parameter (Unit)	Value
T_E (K)	493.3
m_{Sn} (K/wt pct)	–2.9912
$m_{\text{Ag}_3\text{Sn}}$ (K/wt pct)	18.02
C_E (wt pct)	3.73
D (m ² s ⁻¹)	9.08×10^{-10}
Γ_{Sn} (K m)	8.6×10^{-8}
$\Gamma_{\text{Ag}_3\text{Sn}}$ (K m)	10.2×10^{-8}
K_1 (K s m ⁻²)	1.79×10^{10}
K_2 (K m)	24.62×10^{-8}
ϕ (-)	1.9 – 3.68

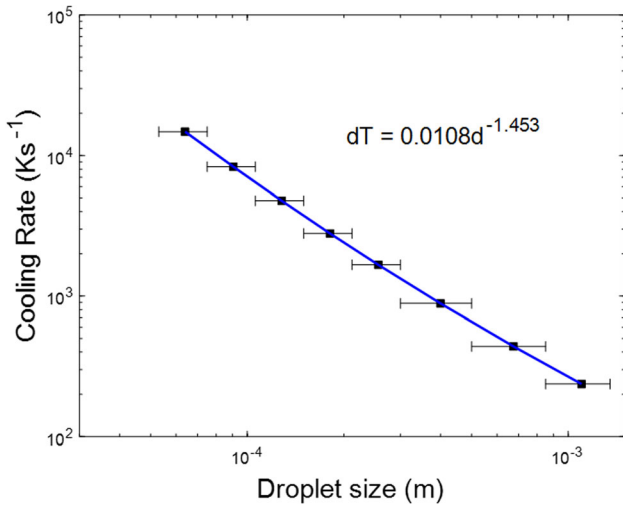


Fig. 2—Estimated cooling rate of Sn-Ag solder in drop tube as a function of droplet size.

850–38 μm size range, with cooling rates range from 250 to 14,800 K s^{-1} .

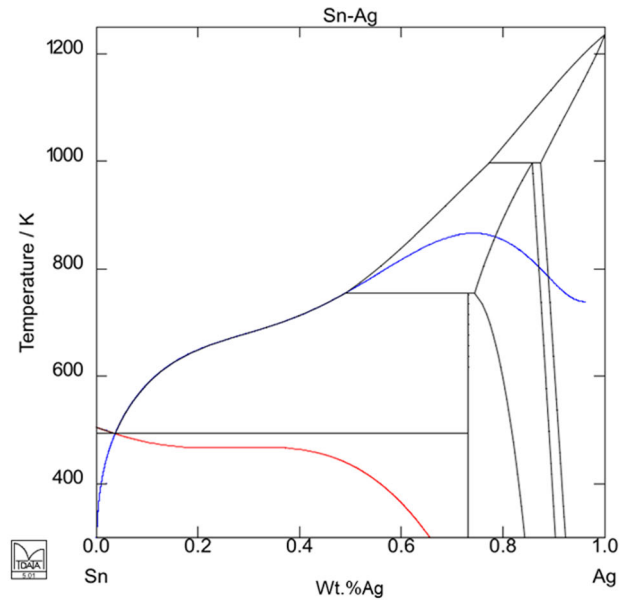
Erol *et al.*^[43,54] have also estimated cooling rates in the drop tube, finding the same general trend as observed here. However, our cooling rates are significantly lower than those in their experiments. The main factor contributing to this difference is the lower melting point of our alloy compared to the relatively high melting point materials considered by Erol *et al.* The relationship between the cooling rate and the droplet diameter obtained by power-law fitting may be expressed as follows:

$$\frac{dT}{dt} = 0.0108 \times d^{-1.453}, \quad [11]$$

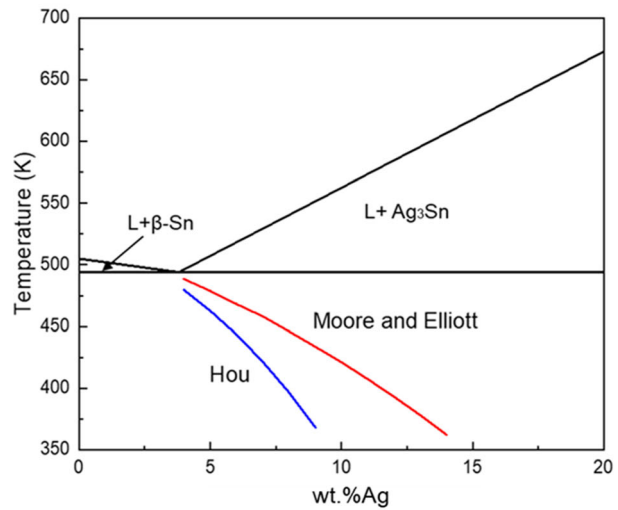
where both d and $\frac{dT}{dt}$ are in standard SI units.

The metastable extensions of the $\beta\text{-Sn}$ and Ag_3Sn liquidus lines, as calculated using MTDATA, are shown in Figure 3(a). The most notable feature of these extensions is that the line for $\beta\text{-Sn}$ changes gradient so as to become essentially flat just below the eutectic temperature. The implication of this is that potentially very large enrichments in the Ag concentration of the liquid may be achievable for a relatively small increase in undercooling. Conversely, the extension of the Ag_3Sn liquidus line proceeds with a gradient similar to that displayed above the eutectic temperature.

The dendritic and eutectic growth models outlined in Eqs. [5] through [9] were used to determine the boundary of the coupled zone on the Sn-rich side of the phase diagram. As can be seen from Equations [7] through (9), the value of the eutectic growth velocity depends upon ϕ , where the estimated value for Sn-Ag₃Sn is likely to fall in the range 1.9–3.68.^[47,53] The resulting locations for the boundary of the coupled zone on the Sn-rich side of the eutectic are shown in Figure 3(b). It may be seen that as the value of ϕ increases, the coupled zone is skewed more towards the Ag₃Sn side of the eutectic.



(a)



(b)

Fig. 3—(a) The Sn-Ag phase diagram, including metastable extensions to the $\beta\text{-Sn}$ and Ag_3Sn liquidus lines, as calculated by the CALPHAD program MTDATA and (b) Location of the Sn-rich side of the coupled zone for different values of the eutectic operating parameter, ϕ .

B. Experimental Results

One of the potential issues when working with Ag bearing melts is loss of Ag through volatilization. This may be particularly the case when working with fine powders due to the high area to mass ratio displayed by such powders, although their high cooling rate, and hence, short time at elevated temperatures, may tend to mitigate against this. For this reason, quantitative EDX area analysis was performed on all size fractions of the drop-tube powders, with the results being shown in Figure 4. The average Ag content of the droplets is approximately 4.67 wt pct, with the variation between size fractions being consistent with experimental error,

showing no evidence for systematic loss of Ag. This value is also consistent with that found for the starting material. It is not clear whether the enrichment over nominal of the commercial alloy was inadvertent or deliberate in order to compensate for Ag loss during typical soldering operation. In any case, the alloy is slightly more hypereutectic than suggested by the nominal composition.

Figure 5 shows an SEM backscatter image of a region of the hypereutectic Sn–Ag ingot. On the assumption of close to equilibrium solidification for the ingot, we might have expected a solidification structure as predicted by the phase diagram, namely proeutectic Ag_3Sn , followed by the transformation of the remaining liquid into a eutectic structure. In fact, it is clear that this is not the case, with the primary solidification phase, even close to equilibrium, being dendritic $\beta\text{-Sn}$, with an interdendritic eutectic.

Figure 6 gives SEM backscatter images of drop tube powders from four different size fractions, namely 850-500, 212-150, 106-75, and $< 38 \mu\text{m}$. The overall form of the microstructure is similar in all four cases shown (and indeed, in that of the other size fractions, which due to the similarities to the structures given in Figure 6, were obtained but have not been presented). In all cases, the primary solidification phase is that of $\beta\text{-Sn}$ dendrites, with an interdendritic eutectic. The dendritic morphology is particularly evident in part b of Figure 5, where to the top right of the image, a split primary trunk with secondary arms is evident. The presence of $\beta\text{-Sn}$ as the primary solidification phase is in agreement with previous work on rapidly quenched near eutectic Sn–Ag alloys.^[55] The other feature that is evident from Figure 6 is that as the cooling rate increases, there is an apparent decrease in the volume fraction of the interdendritic eutectic. Again, this is in accord with previous work

with, for instance, Ochoa and co-workers^[29,56] reaching similar conclusions.

Given the relatively clear delineation between the $\beta\text{-Sn}$ dendrites and the interdendritic eutectic, image analysis using ImageJ was employed to determine the relative area fractions of the two phases, which in turn, give a random distribution of the phases, the best estimator of their relative volume fractions. Due to the tiny size of intermetallic, we could only distinguish the region of eutectic for droplet larger than $106 \mu\text{m}$. The result of this determination, expressed in volume fraction eutectic as a function of estimated cooling rate, is given in Figure 7 for all size fractions of powder obtained from the drop tube, not just the four as shown in Figure 6. This confirms that as the cooling rate increases, the eutectic fraction gradually decreases. For the droplets $> 850 \mu\text{m}$, the eutectic content is approximately 36 vol pct, dropping to 28 vol pct for the $150\text{-}106 \mu\text{m}$ droplets.

Given that the starting alloy is hypereutectic, the relatively small volume fractions of eutectic present in the drop-tube powders must imply that the concentration of Ag in the eutectic regions is significantly in excess of its equilibrium value. In order to quantify this, an iterative mass balance calculation was performed. We start from an initial estimate of the Ag concentration for the eutectic region, from which we can then calculate the mole and mass fractions of Sn and Ag_3Sn . Implicit within this calculation is the assumption that, as at equilibrium, there is zero solubility of Ag in the $\beta\text{-Sn}$ dendrites, a point we return to below. Knowing the ratio of Ag_3Sn to Sn in the eutectic, we can then convert the measured volume fraction of eutectic to a mass fraction, for which we assume densities of 9630 and 7310 kg m^{-3} for Ag_3Sn and Sn, respectively. With a calculated mass fraction of eutectic, it is then a straightforward matter to apply a mass balance to determine the Ag concentration

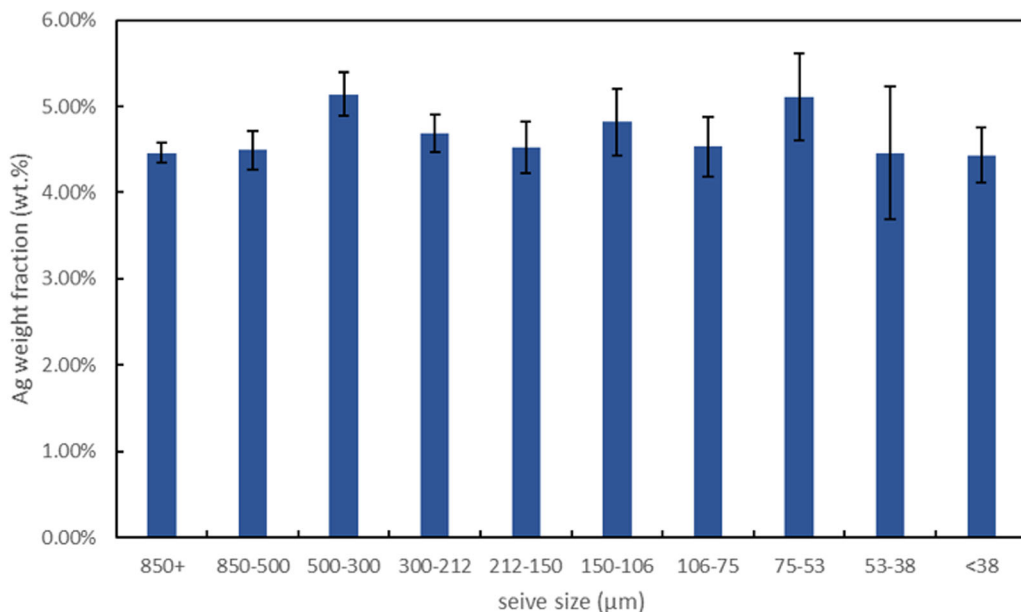


Fig. 4—EDX characterization of Ag content in droplets.

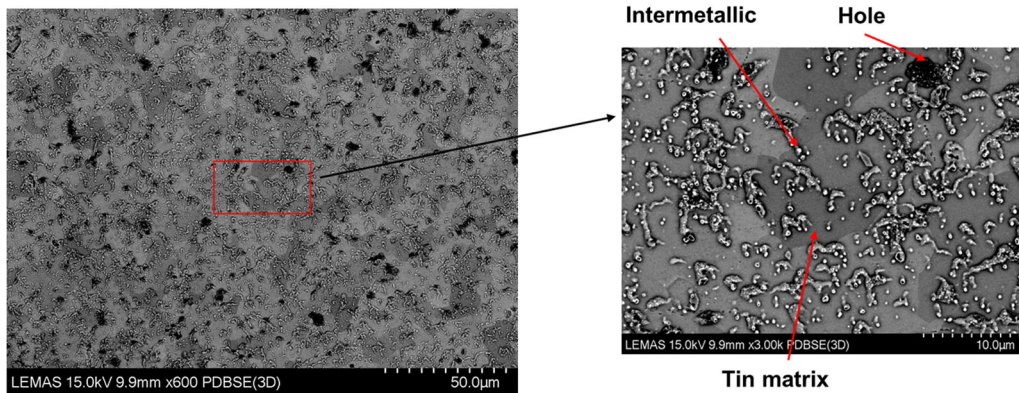


Fig. 5—SEM-backscattered image of the hypereutectic Sn–Ag starting ingot.

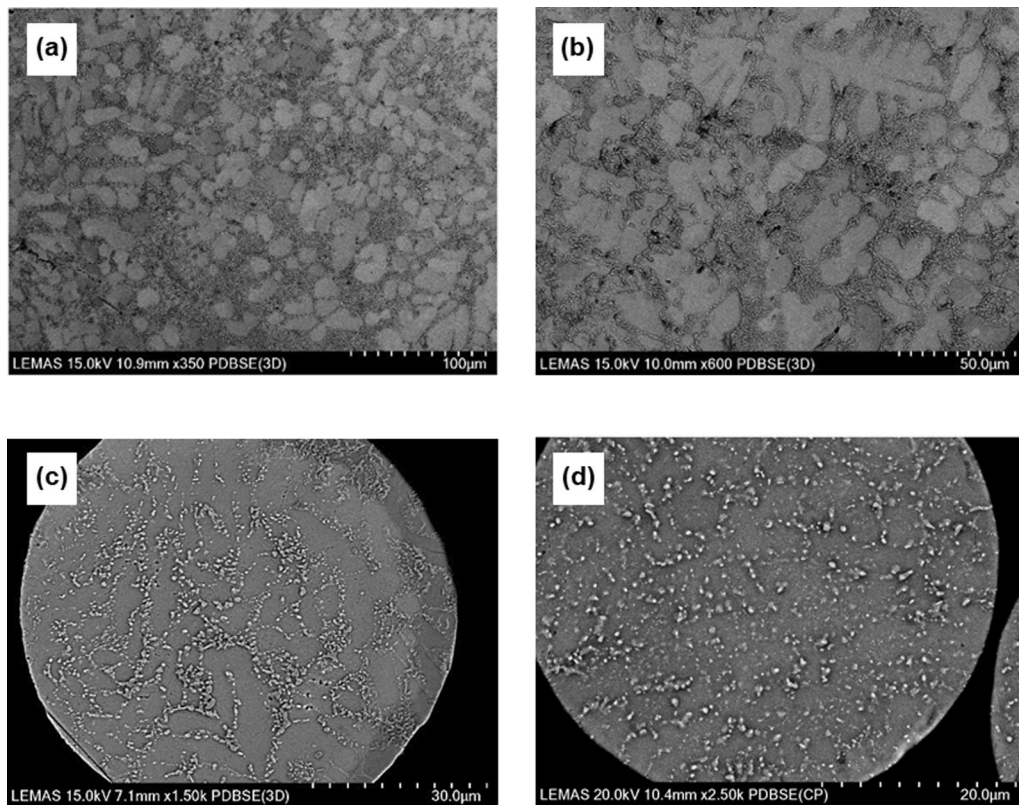


Fig. 6—BSE image of hypereutectic Sn–Ag droplets produced by drop tube. From top to bottom: (a) 850–500 μm , (b) 212–150 μm , (c) 106–75 μm , and (d) < 38 μm droplets.

of the eutectic region, with this value forming the initial estimate of the Ag concentration for the next iteration of the calculation; the iteration is performed on the density of the eutectic region depending upon the relative fractions of Ag_3Sn and $\beta\text{-Sn}$. The calculation stops when the initial and final estimates of the Ag concentration from a given iterative cycle agree to within a predefined tolerance, taken here a 0.01 wt pct. Convergence invariably occurs within 2–3 iterations. The results of this calculation, for all drop-tube size fractions, are shown in Figure 8. As expected, the lower volume fraction of eutectic at high cooling rate leads to a higher determined Ag concentration within the eutectic region,

with values from 12.5 wt pct Ag for the > 850 μm sieve fraction, to > 15 wt pct Ag for the 150–106 μm size fraction. All values are, as expected, considerably in excess of the eutectic at 3.8 wt pct Ag.

As mentioned above, implicit within the mass balance calculation is the assumption that there is essentially zero solubility of Ag in the $\beta\text{-Sn}$ dendrites, which is true under equilibrium conditions. However, it is important to consider the potential influence of solute trapping due to rapid solidification. This is especially the case in small-sized droplets, which will be subject to the highest cooling rates (and undercoolings), and hence, the highest growth velocities. For this reason, the < 38 μm

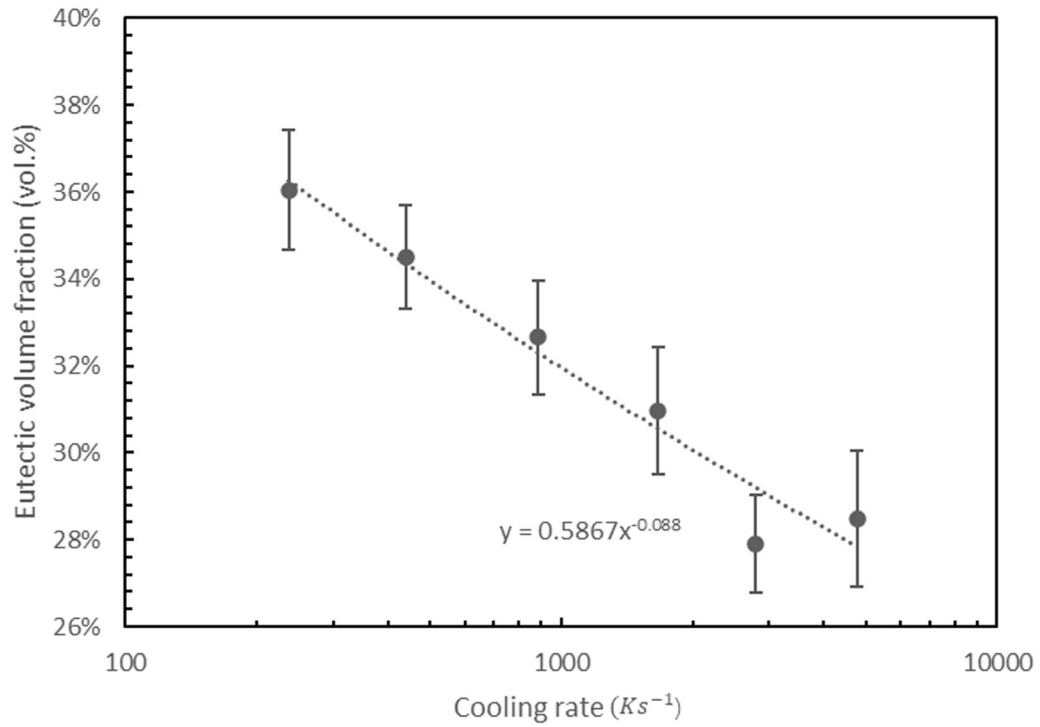


Fig. 7—Variation of eutectic volume fraction with cooling rate.

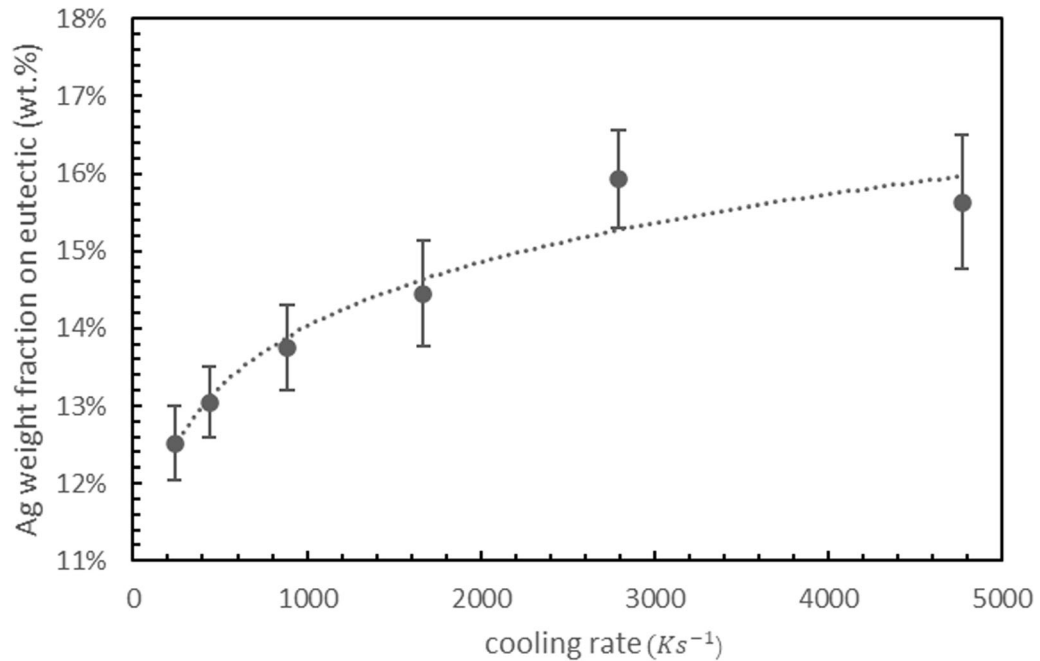


Fig. 8—Relationship between cooling rate and Ag concentration in the eutectic region.

droplets are preferentially observed; if solute trapping is not detected in the smallest droplets, solute trapping is highly unlikely in the larger size fractions. Figure 9(a) presents an example of an EDX line scan conducted on Sn dendritic structures in a $< 38 \mu\text{m}$ droplets. Ten areas displaying dendritic structures were analyzed, and all line scan results showed no Ag present within the β -Sn

dendrites at a level above which we ascribe to noise associated with the EDX detector. In addition, EDX area scans were also performed within the Sn dendritic structures, with the results similarly indicating that the scanned areas contained no Ag. We, therefore, have confidence in the assumption behind the mass balance calculation that all the Ag is contained within the

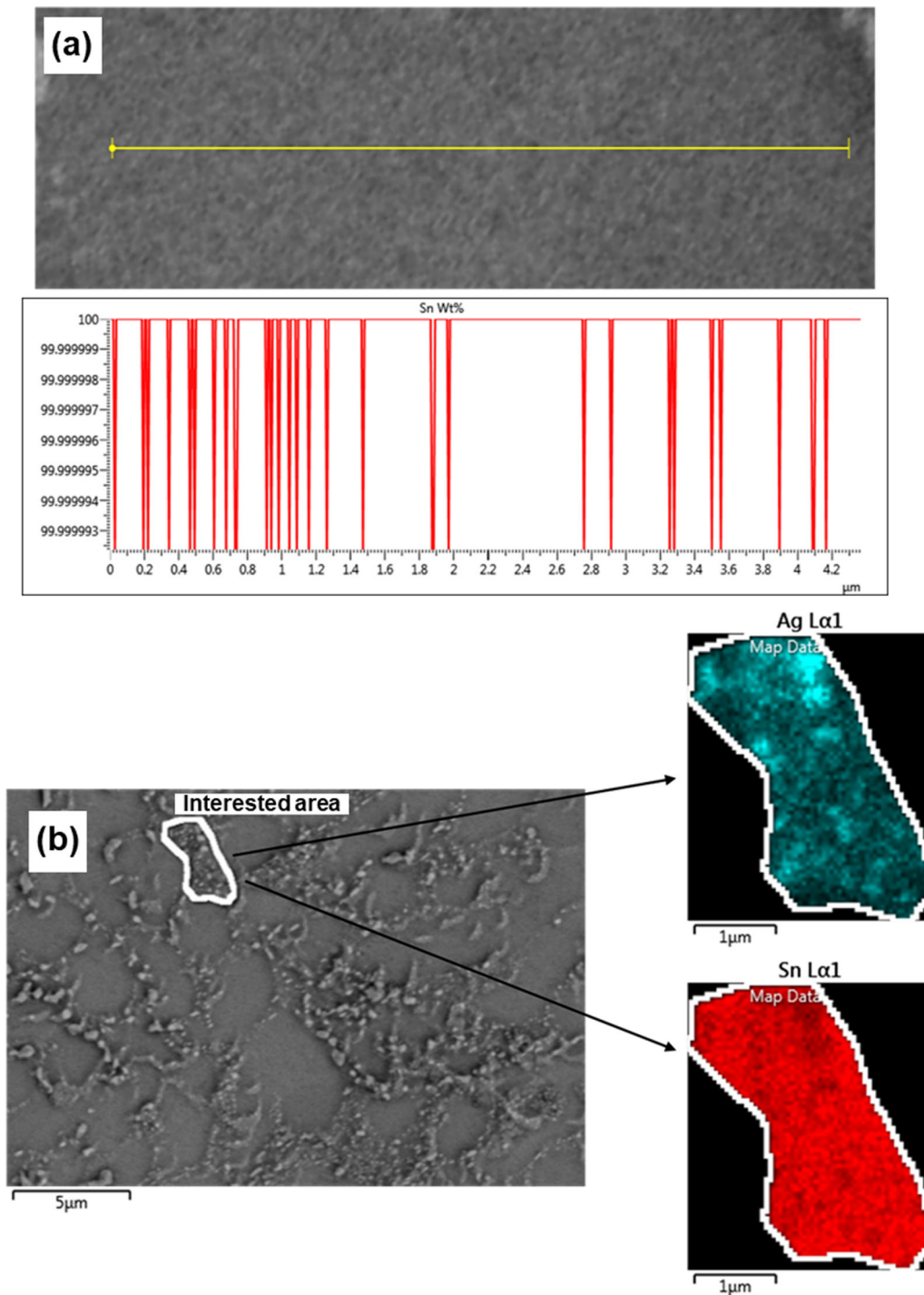


Fig. 9—(a) EDX line scan of a Sn dendritic in a < 38 μm droplet, (b) EDX map scan of eutectic area within a 75-53 μm droplet.

eutectic regions. Furthermore, Figure 9(b) shows an EDX map for a selected region of eutectic within a 75-53 μm droplet, the eutectic area containing 14.34 wt pct Ag, consistent with the high Ag concentration obtained *via* the mass balance calculation.

Given that the Ag concentration of the eutectic regions is so far in excess of the equilibrium eutectic, we consider it prudent to investigate the distribution of the Ag₃Sn within these regions to determine whether it

accords with the rod-like eutectic morphology expected for this system. For this, high-resolution SEM, TEM on FIB-milled thin sections, and thermal analysis have been undertaken. Figure 10 presents high-resolution backscatter SEM micrographs of the < 38, 75-106, 106-150, and 150-212 μm size fractions. The microstructure of the 150-212 μm powders exhibits dendrites surrounded by interdendritic eutectic, consistent with those reported by other studies on similar

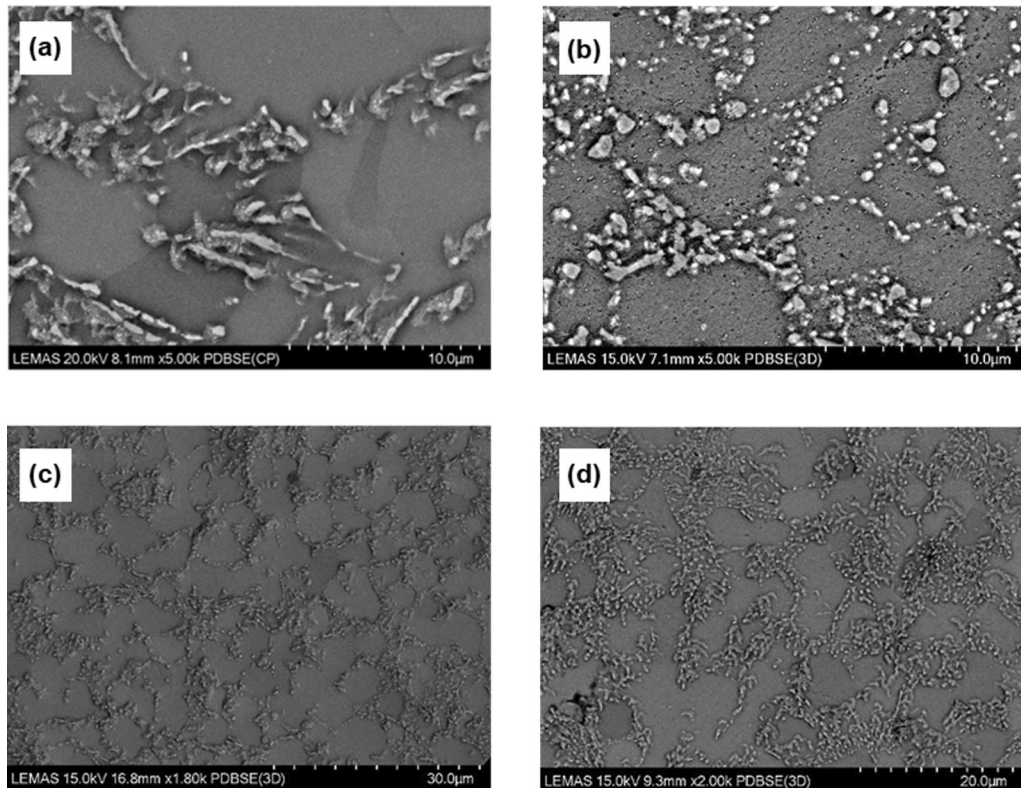


Fig. 10—Microstructure of bulk intermetallic (a) $< 38 \mu\text{m}$ droplets, (b) $106 - 75 \mu\text{m}$ droplets, (c) $150 - 106 \mu\text{m}$ droplets, and (d) $212 - 150 \mu\text{m}$ droplets.

materials.^[29,30,55] In contrast, from the $106\text{--}150 \mu\text{m}$ sample and downwards in powder size (broadly for cooling rate $> 4770 \text{ K s}^{-1}$), we see large, isolated regions of Ag_3Sn , which appear bright in the backscatter images due to the higher atomic number of Ag, relative to Sn. These appear much more akin to either divorced eutectic or proeutectic Ag_3Sn . Moreover, as shown in Figures 10(a) and (b), as the droplet size decreases, the content of this proeutectic intermetallic also increases.

Focused Ion Beam (FIB) was utilized to section areas of interest in droplets of various size ranges, followed by analysis of these regions through Transmission Electron Microscopy (TEM), as shown in Figure 11. The TEM images clearly display grain boundaries, allowing for the distinction between Sn grains and regions of residual liquid that is subsequently solidified to eutectic. Moreover, a clear distinction is apparent between the larger droplets which contain numerous small Ag_3Sn regions with a quasi-regular spacing consistent with the appearance of an irregular rod-like eutectic and the smaller droplets which contain a much smaller number of larger Ag_3Sn regions, with seemingly preferential nucleation on the grain boundaries. In this regard, the absence of neatly arranged rod-like phases and the presence of Sn matrix surrounding the intermetallic are more suggestive of the residual liquid forming a divorced-like eutectic structure. Conversely, in the larger droplets, although we still observe proeutectic intermetallic near the Sn grain boundaries, we also observe a neatly arranged rod-like phase structure surrounding these, wherein we

believe that the proeutectic intermetallic is possibly surrounded by rod-like eutectic. On this assumption, it is also possible from Figure 11 to determine the average rod spacing, $\lambda_a = 0.606 \mu\text{m}$, which can be compared to the extremum spacing, λ_e , calculated using Equations [7] through [9] in order that the operating parameter, ϕ , can be determined. The results of this calculation are given in Table III, wherein we also note that the value of $\lambda_a^2 V$ found is similar to that used by Hou *et al.*^[53] The TEM-SAED pattern for Ag_3Sn along the $[1\bar{1}0]$ zone axis is shown in Figure 11(d). The pattern is identified as being HCP, wherein forbidden reflections occur when $h + 2k = 3n$ and l is odd. However, many such superlattice spots are evident in the SAED pattern, indicating extensive chemical ordering. Hou *et al.*^[53] notes that the crystal structure of Ag_3Sn is orthorhombic, which deviates from our result. However, the result from Cui *et al.*^[57] shows the extremely close correspondence between the cell angles of the $\text{D}0_a$ structure and standard HCP. Moreover, as the $\text{D}0_a$ structure is a chemically ordered derivative of the HCP structure with a small orthorhombic distortion^[57,58] distinguishing these two structures is notoriously difficult.

Further information about the nature of the sample can be obtained from Differential Scanning Calorimetry (DSC). The heating regime, as discussed in more detail in the methodology section, was designed to facilitate a very slow heating rate through the eutectic point during a single heating cycle. Typical DSC traces for large ($850\text{--}500 \mu\text{m}$) and small ($106\text{--}75 \mu\text{m}$) droplets are shown

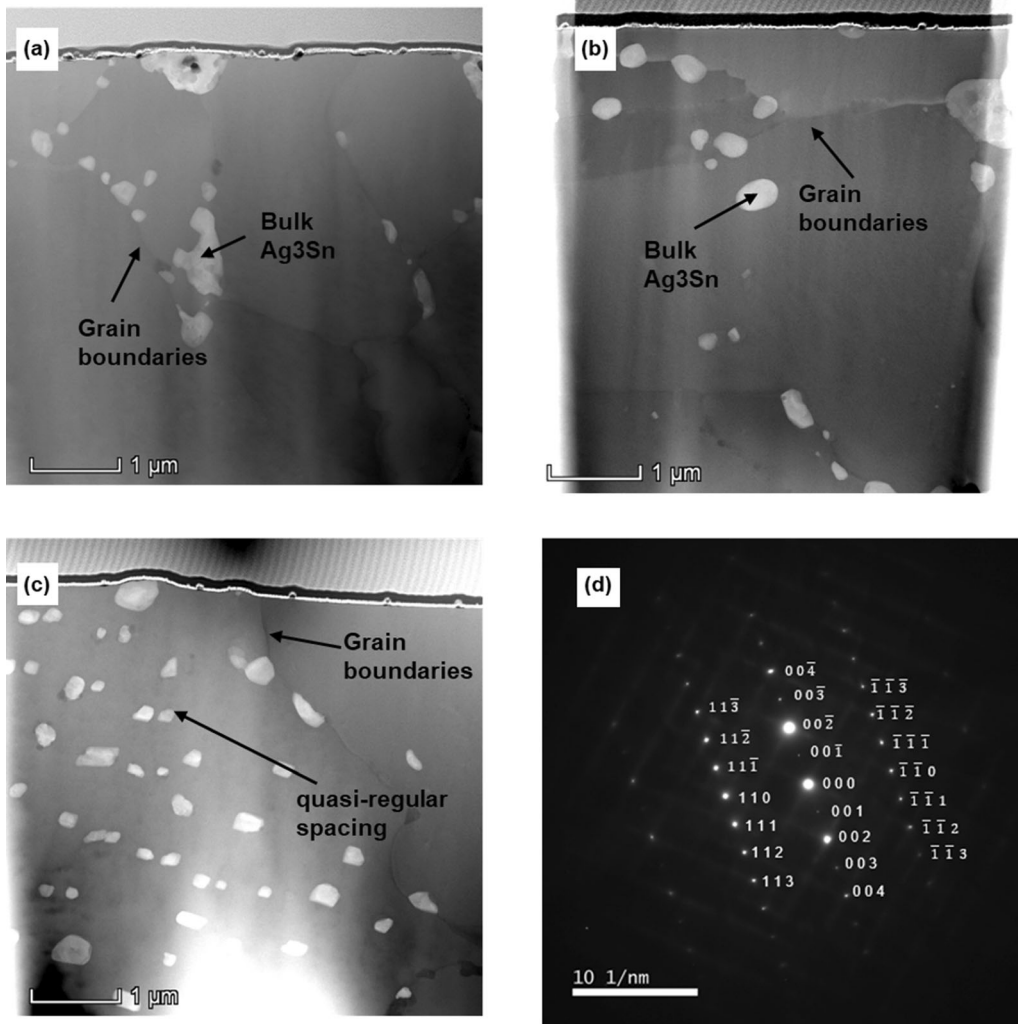


Fig. 11—FIB/TEM image of interested area: (a) $< 38 \mu\text{m}$ droplets, (b) $106 - 75 \mu\text{m}$ droplets, and (c) $500 - 300 \mu\text{m}$ droplets. d Selected area electron diffraction pattern (SAED) along $[1\bar{1}0]$.

Table III. Spacing-Velocity-Undercooling Relationship in Sn-Ag Alloys for 300-500 μm Droplets (Parameters for Calculation as Given in Given in Table II)

Parameter (Unit)	Value
λ_a (μm)	0.606
λ_e (μm)	0.265
ϕ (-)	2.287
V ($\mu\text{m/s}$)	195.859
ΔT (K)	2.72
$\lambda_a \sqrt{V} \left(\frac{\text{m}^{1.5}}{\text{s}^{0.5}} \right)$	8.481

in Figure 12, wherein clear differences between the traces may be observed. In particular, the trace for the large droplets can be resolved into 4 distinct sub-peaks, whereas the trace for the small droplets consists of a single dominant peak with a very small blip at its high-temperature end. Although for the sake of brevity not all DSC traces are shown, this is consistent with the general trend we observe, wherein the number of

sub-peaks, and the extent to which each is resolved, decreases as the cooling rate increases (or equivalently the droplet size decreases).

The most likely explanation for multiple sub-peaks in the trace for the large droplet would be a much greater variety of sizes of Ag_3Sn within the microstructure, wherein the Gibbs-Thomson effect means that structures of higher curvature, *i.e.*, a finer dispersion of phases, would result in a slightly lower melting temperature. Conversely, in the smaller droplets, a single melting peak would be indicative of a more uniform distribution of Ag_3Sn phase within the microstructure. This would be consistent with the picture from SEM and TEM analysis in which large droplets appear to have proeutectic (or divorced eutectic Ag_3Sn) in a matrix of finer rod-like eutectic whereas in the smaller droplets, all of the Ag_3Sn appears to be in proeutectic (or divorced eutectic) particles. Moreover, as the smaller droplets are generally scale refined relative to their larger counterparts, a larger Gibbs-Thomson depression of the melting temperature would account for the lower temperature

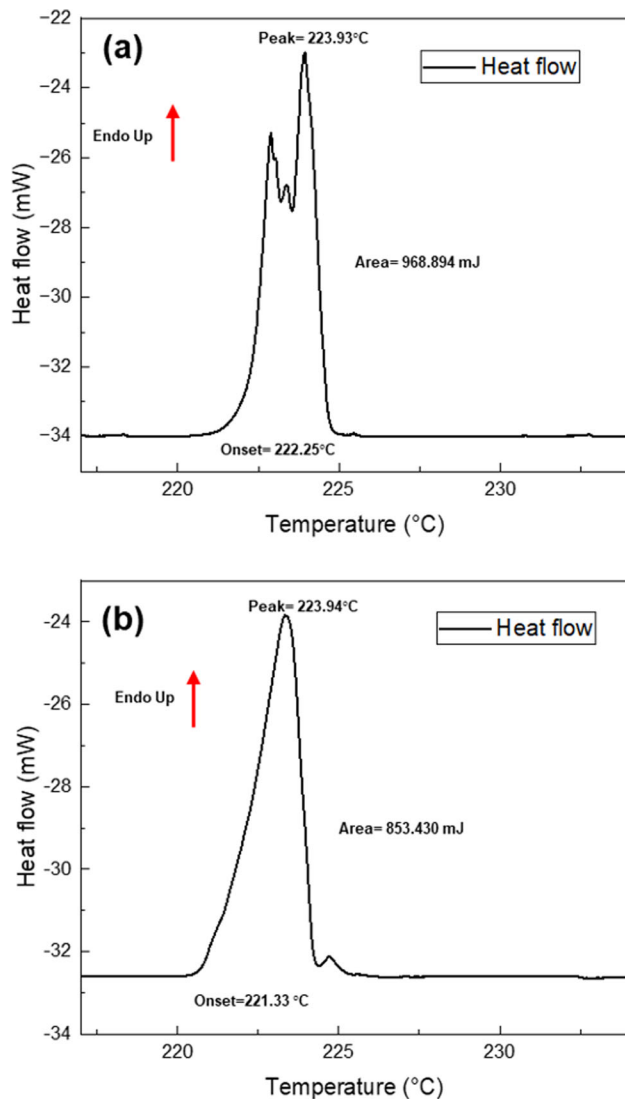


Fig. 12—(a) DSC result of (a) 850-500 μm , (b) 106-75 μm droplets.

for the onset of melting observed when comparing Figures 12(a) and (b).

The total melting enthalpy represented in Figure 12(a) for the 850-500 μm sample is 968.89 mJ, which for a 15.10 mg sample equates to 64.2 J g^{-1} , while for the 106-75 μm sample shown in Figure 12(b), we have an enthalpy of 941.94 mJ for a sample mass of 14.69 mg, equating to 64.1 J g^{-1} . This compares with a range of $56.1\text{--}64.9 \text{ J g}^{-1}$, which has previously been determined for the Sn-Ag eutectic^[59-64], with the value given in this work being towards the top end of this range, probably because the alloy used is somewhat hypereutectic. For information, a peak deconvolution of Figure 12(a) has been undertaken using the program OriginPro, wherein the four visible peaks correspond (from lowest to highest melting temperatures) to 12.9, 20.0, 15.6, and 51.5 pct of the total mass, respectively, although we do not here attempt to associate these individual melting events with specific types of feature within the microstructure. We also note that in all cases, melting is essentially complete by 225 $^{\circ}\text{C}$ and that there is no tin

melting peak (231.9 $^{\circ}\text{C}$), despite there being large pure $\beta\text{-Sn}$ dendrites throughout the microstructure. This is consistent with the bulk composition of the alloy, wherein dissolved Ag within the melt would facilitate melting at, or near, the eutectic temperature.

IV. DISCUSSION

The results of our investigation can be summarized as follows. The primary solidification phase is $\beta\text{-Sn}$ dendrites, not proeutectic Ag_3Sn . This is in line with previous studies of Sn-Ag solder alloys at high cooling rate^[65-67] and is consistent with the calculated coupled zone (Figure 3(b)), in which the $\beta\text{-Sn}$ /eutectic boundary is skewed significantly towards the intermetallic phase. Following growth of this primary $\beta\text{-Sn}$, the residual liquid attains very considerable enrichment in Ag before precipitation of Ag_3Sn . These values reach 12.5 wt pct Ag for the lowest drop-tube cooling rates and > 15 wt pct Ag for the fastest cooling particles. With reference to the calculated eutectic-coupled zone, this would imply a very significant undercooling is being achieved, with an Ag concentration of 15 wt pct implying a depression below the eutectic temperature of 145 K, even when taking the more favorable of the boundaries shown in Figure 3(b). Given that this would represent about 0.3 of the absolute melting temperature, this is a very high undercooling to achieve in a low melting point material at what are relatively modest cooling rates. Once growth of Ag_3Sn is initiated, the morphology is that of a proeutectic phase. This would be consistent with the very high Ag supersaturation attained by the residual liquid. Following a period of proeutectic Ag_3Sn growth, the slower cooling particles appear to swap to a more conventional $\text{Ag}_3\text{Sn}/\beta\text{-Sn}$ irregular rod-like eutectic morphology, the operating point parameter for which has been determined as $\phi = 2.3$ in the case of 500-300 μm particles. However, for the faster cooling droplets, growth of Ag_3Sn continues with a more proeutectic (or divorced eutectic) type morphology. These two mechanisms are shown in Figure 13.

These results are significantly different from many of the previous studies on the solidification morphology of Sn-Ag solders, a fact that we postulate may be due to the role of Ag_3Sn nucleation kinetics. Many of the previous studies on this system have used Bridgman growth^[29-32] wherein all phases are allowed to nucleate before the main period of growth, which is typically the object of such studies. Conversely, in a freely falling droplet, little time is available for nucleation, and very different results may be obtained if one of the phases (Ag_3Sn) is difficult to nucleate. In this respect, we note the rather anomalous form of the metastable extension of the Sn liquidus line, which becomes almost flat $\approx 25 \text{ K}$ below the eutectic temperature. The implication is that the very significant Ag enrichment that we observe as having occurred in the residual liquid following growth of $\beta\text{-Sn}$ dendrites, could have occurred at very modest undercoolings.

Of course, as the Ag concentration increases, the driving force for nucleation of Ag_3Sn would also increase, leading to the formation of a blockier, less

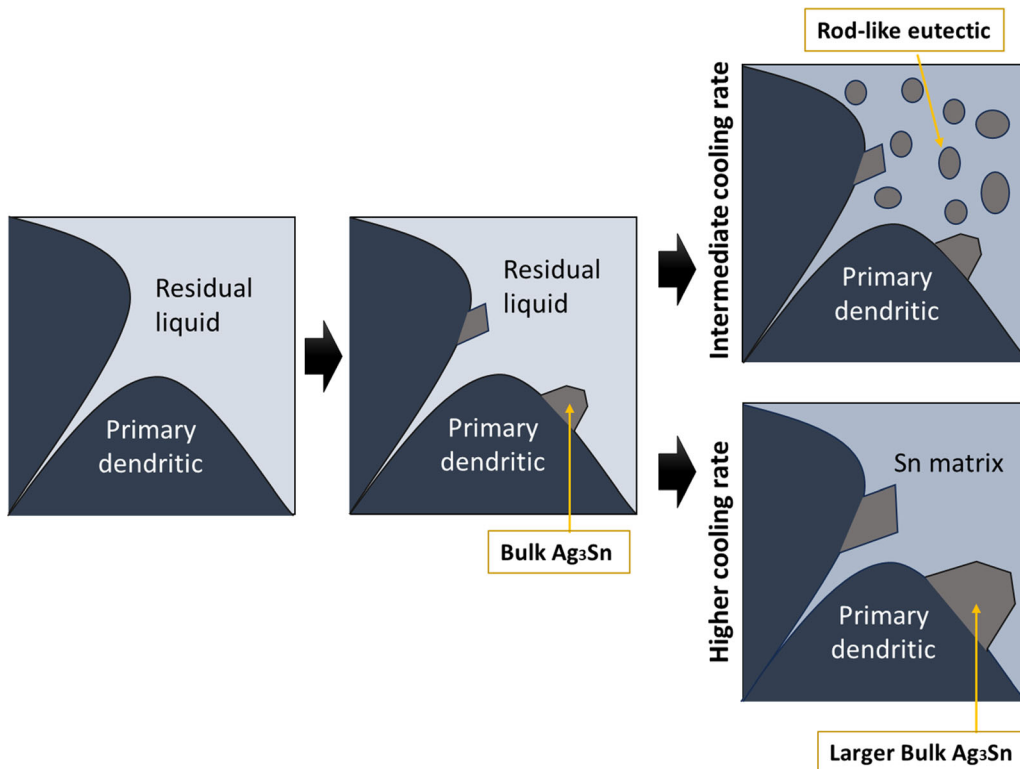


Fig. 13—Two schematic Ag_3Sn growth mechanism following initial nucleation upon $\beta\text{-Sn}$ grain boundaries: rod-like eutectic formed at intermediate cooling rate and further growth of the divorced-like eutectic at higher cooling rate.

rod-like eutectic morphology. Heterogeneous nucleation would be favored on the preexisting $\beta\text{-Sn}$, wherein we observe Ag_3Sn clustered around the $\beta\text{-Sn}$ grain boundaries, consistent with the TEM observations. As the Ag concentration of the residual liquid drops, we would expect that we would enter the eutectic-coupled zone (from the intermetallic side), wherein the remainder of the liquid would solidify isothermally to the $\beta\text{-Sn}/\text{Ag}_3\text{Sn}$ rod-like eutectic, and at lower cooling rates, this does indeed appear to be what happens. At higher cooling rates, however, we do not see the regions between the proeutectic Ag_3Sn being infilled with eutectic, and we presume that the difficulty in nucleating the Ag_3Sn phase means that continued growth on preexisting proeutectic particles is favored. In this respect, this would be similar to the situation observed by Liao *et al.*^[41] in A390 alloy. This would be consistent with both the TEM observations and DSC experiments, which show multiple melting events for the large droplets but only a single melting event for the smaller droplets. These multiple melting events we interpret as resulting from the presence of different sized Ag_3Sn particles, arising from the proeutectic and the subsequent infill with the rod-like eutectic.

V. SUMMARY AND CONCLUSIONS

At modestly elevated cooling rates, we find that the microstructure of rapidly solidified, hypereutectic Sn–Ag solder alloy is markedly different from that

expected with reference to the phase diagram. At all cooling rates, $\beta\text{-Sn}$ dendrites are observed as the primary solidification phase with an interdendritic eutectic, the volume fraction of which is observed to decrease with increasing cooling rate from ≈ 36 vol pct at the lowest cooling rates, to ≈ 28 vol pct at the highest cooling rates, wherein the Ag concentration in the residual liquid is observed to peak at 15 wt pct Ag. This results in Ag_3Sn within the eutectic that has a blocky appearance, more reminiscent of a divorced eutectic, rather than the more conventional rod-like eutectic. These findings may have implications for the microstructure of solder joints subject to cooling rates of, more than a few 10^3 's of Kelvin per second.

ACKNOWLEDGMENTS

The authors are grateful to the support from Technical Group of the Materials for a Sustainable Future at the University of Leeds. Special thanks are given to Mr Robert Simpson at this group of his kind assistance for characterization and training.

CONFLICT OF INTEREST

The corresponding author, on behalf of all authors, declares that there is no conflict of interest.

OPEN ACCESS

This article is licensed under a Creative Commons Attribution 4.0 International License, which permits use, sharing, adaptation, distribution and reproduction in any medium or format, as long as you give appropriate credit to the original author(s) and the source, provide a link to the Creative Commons licence, and indicate if changes were made. The images or other third party material in this article are included in the article's Creative Commons licence, unless indicated otherwise in a credit line to the material. If material is not included in the article's Creative Commons licence and your intended use is not permitted by statutory regulation or exceeds the permitted use, you will need to obtain permission directly from the copyright holder. To view a copy of this licence, visit <http://creativecommons.org/licenses/by/4.0/>.

REFERENCES

1. H. Tanaka: *Espec technology report* 2002, vol. 14.
2. M. Abtew and G. Selvaduray: *Mater. Sci. Eng. R*, 2000, vol. 27, pp. 95–141.
3. H. Jones and W. Kurz: *Metall. Trans. A*, 1980, vol. 11A, pp. 1265–73.
4. M.H. Burden and J.D. Hunt: *J. Cryst. Growth*, 1974, vol. 22, pp. 328–30.
5. W. Kurz and D.J. Fisher: *Int. Metals Rev.*, 1979, vol. 24, pp. 177–204.
6. G.A. Chadwick: *Prog. Mater. Sci.*, 1965, vol. 12, pp. 99–182.
7. M. Rappaz and J. A. Dantzing: In *solidification*, EPFL Press: 2009, pp 381–89.
8. M. Tassa and J.D. Hunt: *J. Cryst. Growth*, 1976, vol. 34, pp. 38–48.
9. K. Jackson: *Liquid Metals and Solidification*, Cleveland, ASM, 1958, pp. 174–274.
10. R.S. Fidler, M.N. Croker, and R.W. Smith: *J. Cryst. Growth*, 1972, vol. 13(14), pp. 739–46.
11. M.N. Croker, R.S. Fidler, and R.W. Smith: *J. Cryst. Growth*, 1971, vol. 11, pp. 121–30.
12. M.N. Croker, D. Baragar, and R.W. Smith: *J. Cryst. Growth*, 1975, vol. 30, pp. 198–212.
13. M.N. Croker, M. McParlan, D. Baragar, and R.W. Smith: *J. Cryst. Growth*, 1975, vol. 29, pp. 85–97.
14. M.R. Taylor, R.S. Fidler, and R.W. Smith: *J. Cryst. Growth*, 1968, vol. 3–4, pp. 238–43.
15. R. Elliott: *Eutectic Solidification Processing: Crystalline and Glassy Alloys*, Elsevier, New York, 2013.
16. U. Büyük and N. Maraşlı: *Mater. Chem. Phys.*, 2010, vol. 119, pp. 442–48.
17. D.K. Mukhopadhyay, C. Suryanarayana, and F.H. Froes: *Metall. and Mater. Trans. A.*, 1995, vol. 26A, pp. 1939–46.
18. G. Li, E. Brodu, J. Soete, H. Wei, T. Liu, T. Yang, W. Liao, and K. Vanmeensel: *Addit. Manuf.*, 2021, vol. 47, 102210.
19. X. Wang, L. Yang, H. Tan, F. Yu, and J. Cui: *Int. J. Cast Met. Res.*, 2022, vol. 35, pp. 131–38.
20. V. Bathula, C. Liu, K. Zwejack, J. McKeown, and J.M. Wierzok: *Acta Mater.*, 2020, vol. 195, pp. 341–57.
21. H. Wang, Y. An, X. Xu, X. Guo, and Y. Hu: *Mater Charact*, 2020, vol. 170, 110703.
22. Y. An, X. Xu, L. Liang, Y. Zhao, and H. Hou: *J. Alloys Compd.*, 2021, vol. 864, p. 158821.
23. Y. An, L. Liang, X. Xu, Y. Zhao, and H. Hou: *J. Market. Res.*, 2021, vol. 11, pp. 548–63.
24. X. Xu, C. Tang, H. Wang, Y. An, and Y. Zhao: *J. Mater. Sci. Technol.*, 2022, vol. 128, pp. 160–79.
25. M.R. Abul, R.F. Cochrane, and A.M. Mullis: *J. Mater. Sci. Technol.*, 2022, vol. 104, pp. 41–51.
26. X. Qi, N. Takata, A. Suzuki, M. Kobashi, and M. Kato: *Addit. Manuf.*, 2020, vol. 35, 101308.
27. H.H. Lien, J. Mazumder, J. Wang, and A. Misra: *Mater. Res. Lett.*, 2020, vol. 8, pp. 291–98.
28. B. Wei, W. Wu, D. Xie, H.H. Lien, M. Kayitmazbatir, A. Misra, and J. Wang: *Mater. Res. Lett.*, 2021, vol. 9, pp. 507–15.
29. F. Ochoa, J.J. Williams, and N. Chawla: *JOM*, 2003, vol. 55, pp. 56–60.
30. K.S. Kim, S.H. Huh, and K. Sukanuma: *Mater. Sci. Eng. A*, 2002, vol. 333, pp. 106–14.
31. J.F. Bromley, F. Vnuk, and R.W. Smith: *J. Mater. Sci.*, 1983, vol. 18, pp. 3143–53.
32. M. Şahin and E. Çadrlı: *J. Mater. Sci.*, 2012, vol. 23, pp. 484–92.
33. R.S. Sidhu and N. Chawla: *Mater Charact*, 2004, vol. 52, pp. 225–30.
34. X. Liu, M. Huang, Y. Zhao, C.M.L. Wu, and L. Wang: *J. Alloys Compd.*, 2010, vol. 492, pp. 433–38.
35. D.W. Henderson, T. Gosselin, A. Sarkhel, S.K. Kang, W.K. Choi, and D.Y. Shih: *J. Mater. Res.*, 2002, vol. 17, pp. 2775–78.
36. R.W. Cahn and P. Haasen: *Physical Metallurgy*, Elsevier, New York, 1996, pp. 767–68.
37. C.J. Lin, L. Peng, J.W. Xian, Q. Li, and C.M. Gourlay: *J. Alloys Compd.*, 2023, vol. 938, 168571.
38. J.H. Kang, J. Park, K. Song, C.S. Oh, O. Shchyglo, and I. Steinbach: *J. Magnes. Alloys*, 2022, vol. 10, pp. 1672–79.
39. J. Baral, S. Das, and R. Sarvesha: *Metallogr. Microstruct. Anal.*, 2022, vol. 11, pp. 245–54.
40. G. Du, F. Liu, and J.B. Li: *Mater. Lett.*, 2020, vol. 265, 127406.
41. H. Liao, Y. Wu, H. Chen, and L. Qian: *Metall. Mater. Trans. A*, 2022, vol. 53A, pp. 2346–50.
42. K.A. Jackson and J.D. Hunt: *Dynamics of Curved Fronts*, Elsevier, New York, 1988, pp. 363–76.
43. M. Erol and U. Büyük: *Trans. Indian Inst. Met.*, 2016, vol. 69, pp. 961–70.
44. O. Oloyede, T.D. Bigg, R.F. Cochrane, and A.M. Mullis: *Mater. Sci. Eng. A*, 2016, vol. 654, pp. 143–50.
45. R.H. Davies, A.T. Dinsdale, J.A. Gisby, J.A.J. Robinson, and S.M. Martin: *Calphad*, 2002, vol. 26, pp. 229–71.
46. N. Hou: Imperial College London: 2019, pp 77–81.
47. A. Moore and R. Elliot: *The Solidification of Metals*, The Iron and Steel Institute, London, 1968, pp. 167–72.
48. E.S. Lee and S. Ahn: *Acta Metall. Mater.*, 1994, vol. 42, pp. 3231–43.
49. J. Lipton, W. Kurz, and R. Trivedi: *Acta Metall.*, 1987, vol. 35, pp. 957–64.
50. G.E. Nash and M.E. Glicksman: *Acta Metall.*, 1974, vol. 22, pp. 1283–90.
51. D.A. Kessler, J. Koplík, and H. Levine: *Phys. Rev. A*, 1985, vol. 31, p. 1712.
52. P. Magnin and W. Kurz: *Acta Metall.*, 1987, vol. 35, pp. 1119–28.
53. N. Hou, J.W. Xian, A. Sugiyama, H. Yasuda, and C.M. Gourlay: *Metall. Mater. Trans. A*, 2023, vol. 54A, pp. 909–27.
54. G. Kasperovich, T. Volkman, L. Ratke, and D. Herlach: *Metall. Mater. Trans. A*, 2008, vol. 39A, pp. 2826–36.
55. J. Shen, Y.C. Chan, and S.Y. Liu: *Intermetallics*, 2008, vol. 16, pp. 1142–48.
56. S.K. Seo, S.K. Kang, D.Y. Shih, and H.M. Lee: *J. Electron. Mater.*, 2009, vol. 38, pp. 718–25.
57. Y. Cui, J.W. Xian, A. Zois, K. Marquardt, H. Yasuda, and C.M. Gourlay: *Acta Mater.*, 2023, vol. 249, pp. 157–68.
58. H. Yu, Y. Sun, W.R. Meier, P.C. Canfield, C.R. Weinberger, S.W. Lee, and M. Aindow: *J. Mater. Sci.*, 2018, vol. 53, pp. 12828–36.
59. J. Pacio and T. Wetzel: *Sol. Energy*, 2013, vol. 93, pp. 280–94.
60. F. Meydaneri and B. Saatçi: *Arab. J. Sci. Eng.*, 2014, vol. 39, pp. 8027–36.
61. E. Çadrlı, M. Şahin, R. Kayalı, M. ArI, and S. Durmuş: *J. Mater. Sci.*, 2011, vol. 22, pp. 1411–21.
62. F. Meydaneri, B. Saatçi, and M. Özdemir: *Kovove Materialy*, 2013, vol. 51, pp. 305–12.
63. P.J. Shamberger, Y. Mizuno, and A.A. Talapatra: *J. Appl. Phys.*, 2017, vol. 122, 215301.
64. C. Morando, O. Fornaro, O. Garbellini, and H. Palacio: *J. Mater. Sci.*, 2014, vol. 25, pp. 2824–34.
65. E. Çadrlı, U. Büyük, S. Engin, H. Kaya, N. Maraşlı, K. Keşlioğlu, and A. Ülgen: *J. Mater. Sci.*, 2010, vol. 21, pp. 72–79.

66. E. Çadirli, U. Büyük, S. Engin, H. Kaya, N. Maraşı, and A. Ülgen: *J. Alloys Compd.*, 2009, vol. 486, pp. 199–206.
67. H. Kaya, E. Çadirli, and M. Gündüz: *J. Mater. Eng. Perform.*, 2003, vol. 12, pp. 417–23.

Publisher's Note Springer Nature remains neutral with regard to jurisdictional claims in published maps and institutional affiliations.